

Effective-mass wave-matching theory for a two-band Wannier system

Patrick Roblin*

Department of Electrical Engineering, The Ohio State University, Columbus, Ohio 43210

Paul Sotirelis

National Center for Supercomputer Applications, 405 North Mathews, Urbana, Illinois 61801

J. Gene Cao

Department of Mathematical Sciences, Michigan Technological University, Houghton, Michigan 49931

(Received 2 September 1997; revised manuscript received 16 January 1998)

In this paper, the effective-mass wave-matching theory for the interface of single tridiagonal band systems is extended to a two-band Wannier system. Within the context of the effective-mass wave-matching theory, the four independent coupling parameters of the two coupled tridiagonal bands system are reduced to a single parameter. The impact of this coupling parameter and also of the transverse energy upon the transmission of electrons in resonant tunneling diodes in such systems is demonstrated for the case where the two-band model represents the Γ and X valleys of the conduction band. A multiband density of states is derived to facilitate the location in space and energy of both the resonant tunneling and Γ - X resonances and antiresonances. To qualify the application of this two-band model to real systems, we compare simulation results obtained with the effective-mass wave-matching theory and a single full-band model, which accounts for long-range interactions. A reasonable agreement on a wide range of incident energies is demonstrated for a GaAs-Al_{0.3}Ga_{0.7}As resonant tunneling diode (RTD) using a noneffective-mass correction and a coupling factor of 0.999. An improved fit is further obtained by relaxing the backward interband coupling to zero. The two-band model and the interface wave-matching procedure developed provides a simple yet realistic approach to account for both noneffective-mass effects and the coupling between the Γ and X or L valleys in the calculation of the transmission and reflection coefficients of RTD devices. Finally, the impact of interface roughness scattering in the presence of Γ - X coupling is studied and both the destruction and creation of antiresonant structures are observed. [S0163-1829(98)04744-4]

I. INTRODUCTION

Resonant tunneling diodes (RTD's) have attracted considerable modeling efforts (see Refs. 1 and 2 for an overview) due to their potential applications in high-speed devices, such as oscillators, amplifiers, harmonic multipliers, and logic elements.³⁻⁵ One of the challenges in the modeling the resonant tunneling diodes arises from the fact that resonant tunneling can take place at very large energies inside the conduction band or deep in the forbidden band in the barriers; tunneling is therefore strongly dependent on the full band-structure of the semiconductors involved. The need to use full-band structures to perform realistic simulations of these devices, has therefore been recognized and several full-band RTD models have been reported.⁶⁻¹¹ However, besides their added complexity, these full-band models also suffer from some limitations. For example the nearest-neighbor tight-binding models⁸⁻¹³ that rely on nearest-neighbor matrix elements, fit well with the valence band but do not accurately represent the conduction band,¹⁴⁻¹⁵ compared to the pseudopotential approach.¹⁶⁻¹⁷ In addition, the accuracy of the Hamiltonian used for the interface in the tight-binding approaches¹⁰⁻¹² and the long-range generalized Wannier picture^{7,18-20} must also be verified. *Ab initio* local-density calculations¹⁷ on short- and long-period AlAs/GaAs superlattices have been used for this purpose, but no such calculations are yet available for resonant tunneling diodes.

In this paper, we focus on the development of an interface theory for a system consisting of two tridiagonal Wannier bands. Since Wannier bands are used, the bands must be decoupled away from the interfaces in the flat band regions. At the interfaces, the wave matching introduces a coupling between the two-bands, and the effective-mass wave-matching theory is extended in Sec. II for this purpose. We then demonstrate an application of this model where the two bands represent the Γ and X valleys of the conduction band. A general current definition for coupled multiband system will be introduced to calculate the transmitted current in arbitrary heterostructures. Note that simple tridiagonal bands are used. Therefore, in the flat band region of the contacts the bands feature a simple cosine dispersion versus the wave vector that will be fitted to the effective mass for small wave vectors. An efficient noneffective-mass correction will also be introduced in Sec. V. A multiband density of states theory will be introduced in Sec. IV to analyze the impact of the interface coupling on the electron system. To qualify the effective-mass wave-matching theory presented, in Sec. V we will compare this model with a single full band Wannier model accounting for long-range interactions. In regards to our above discussion on the interface Hamiltonian, we will limit this comparison to GaAs-Al_{0.3}Ga_{0.7}As RTD's that are made up of very similar semiconductors (Al_{0.3}Ga_{0.7}As and GaAs) for which a reasonable approximate full band interface Hamiltonian can be inferred. Finally, we will consider

in Sec. VI the impact of interface roughness scattering on the resonances and antiresonances in a test RTD.

II. MULTITRIDIAGONAL WANNIER PICTURE

The general Hamiltonian of a multiband tridiagonal system is

$$\sum_{b'=1}^{N_B} \sum_{n'=n-1}^{n+1} H(b, b', n, n', \mathbf{k}_\perp) f(b', n, E, \mathbf{k}_\perp) = E f(b, n, E, \mathbf{k}_\perp),$$

where b is the band index, n the Wannier lattice site, E the total energy, \mathbf{k}_\perp the transverse wave vector, and $f(\cdot)$ the Wannier envelope function.¹⁹ This model represents therefore a system of N_B tridiagonal Wannier bands and envelope functions, which are coupled inside the heterostructures. However, the coupling of the various bands must vanish in the flat band regions of the left and right contact as it is to be expected for a Wannier band model. As any Hamiltonian, Hermiticity must be enforced and this implies that we have

$$H(b, b', n, n', \mathbf{k}_\perp) = H^*(b', b, n', n, \mathbf{k}_\perp).$$

The multiband electron current $J_T(n)$ through the heterostructures is (see the Appendix)

$$J_T(n) = \sum_b \sum_{b'} [j(b, b', n, n+1) + j(b', b, n-1, n)],$$

where $j(b', b, n', n)$ is the elemental current

$$j(b', b, n', n) = \text{Im}[H(b', b, n', n, \mathbf{k}_\perp) f^*(b', n', E, \mathbf{k}_\perp) \times f(b, n, E, \mathbf{k}_\perp)]. \quad (1)$$

In the Appendix, it is demonstrated that the Hermiticity of the Hamiltonian leads to current conservation throughout the heterostructure. This demonstrates the validity of the proposed current definition since the later definition relaxes to the conventional current definition in the contacts where the bands are decoupled (no interband current). The conservation of the current is also verified in the simulator developed. Finally, this current definition permits us to define a transmission coefficient from band i to band j as the transmitted current in band j in the right contact divided by the incident current in the band i in the left contact. For the Γ -valley or X -valley example selected in this paper we will only consider the case where the incident electrons are injected in the Γ valley.

We shall assume that in the flat-band contacts as well as in each semiconductor region away from a material interface,

the Hamiltonian consists of several uncoupled tridiagonal Wannier bands. At a site n the local band structure of the band b is therefore of the form

$$E(b, \mathbf{k}, n) = E_c(b, n) - eV(n) - \frac{\hbar^2}{2a^2 m_b^*(n)} [1 \pm \cos(k_x a)] + \frac{\hbar^2 k_\perp^2}{2m_{b\perp}^*(n)}, \quad (2)$$

where $m_b^*(n)$ and $m_{b\perp}^*(n)$ are the longitudinal and transverse effective masses at site n , k_x the longitudinal wave vector, $V(n)$ the electrostatic potential, and $E_c(b, n)$ the bottom of the band b . Note that $(-)$ in (\pm) is used when the minimum is at Γ and $(+)$ at X . A noneffective-mass correction to this model, which can also handle nonspherical X valleys, will be presented in Sec. V.

III. EFFECTIVE-MASS WAVE MATCHING FOR TWO-BAND WANNIER SYSTEM

In this section, we study the extension of the effective-mass matching technique developed by Kroemer and Zhu²¹ to a system of two coupled Wannier bands (1 and 2) at the junction of materials A and B . Coupling between the two bands is assumed to take place at the heterointerface.

We introduce the following simplified notation for the matrix elements associated with the tridiagonal band of Eq. (2):

$$A_b = H(b, b, n_A, n_A + 1) = H(b, b, n_A, n_A - 1) = \mp \frac{\hbar^2}{2a^2 m_{A,b}^*},$$

$$B_b = H(b, b, n_B, n_B + 1) = H(b, b, n_B, n_B - 1) = \mp \frac{\hbar^2}{2a^2 m_{B,b}^*}, \quad (3)$$

$$H_{A/B,b}(n) = H(b, b, n_{A/B}, n_{A/B}, \mathbf{k}_\perp) = \frac{\hbar^2}{a^2 m_{A/B,b}^*} + E_{c,A/B}(b) - eV(n) + \frac{\hbar^2 k_\perp^2}{2m_{A/B,b\perp}^*},$$

where $n_{A/B}$ is a site in material A/B , $m_{A/B,b}$ the effective mass in the band b of material A/B , and $E_{c,A/B}$ the bottom of the band b in material A/B .

Consider the Hamiltonian shown below for a two-band system at an interface between materials A and B located between site n and $n+1$:

$$H = \left[\begin{array}{ccccccccc|cccccccc} \ddots & & \ddots & & \ddots & & & & & & & & & & & & & & \\ & A_1 & H_{A,1} & A_1 & & & & & & & & & & & & & & & \\ & & A_1 & H_{A,1} & C_{12} & & & & & & C_{13} & C_{14} & & & & & & & \\ & & & C_{21} & H_{B,1} & B_1 & & & & & C_{23} & C_{24} & & & & & & & \\ & & & & B_1 & H_{B,1} & B_1 & & & & & & & & & & & & \\ & & & & & \ddots & \ddots & \ddots & & & & & & & & & & & \\ - & - & - & - & - & - & - & - & - & + & - & - & - & - & - & - & - & - \\ & & & & & & & & & & \ddots & \ddots & \ddots & & & & & \\ & & & & & & & & & & A_2 & H_{A,2} & A_2 & & & & & \\ & & & & & & & & & & & A_2 & H_{A,2} & C_{34} & & & & \\ & & & & & & & & & & & & C_{43} & H_{B,2} & B_2 & & & \\ & & & & & & & & & & & & & B_2 & H_{B,2} & B_2 & & \\ & & & & & & & & & & & & & & \ddots & \ddots & \ddots & \end{array} \right]$$

The Wannier equations at the interface are therefore given by

$$\begin{aligned} A_1 f_A(1, n-1) + [H_{A,1}(n) - E] f_A(1, n) + C_{12} f_B(1, n+1) \\ + C_{13} f_A(2, n) + C_{14} f_B(2, n+1) &= 0, \\ B_1 f_B(1, n+2) + [H_{B,1}(n+1) - E] f_B(1, n+1) + C_{21} f_A(1, n) \\ + C_{23} f_A(2, n) + C_{24} f_B(2, n+1) &= 0, \\ A_2 f_A(2, n-1) + [H_{A,2}(n) - E] f_A(2, n) + C_{34} f_B(2, n+1) \\ + C_{31} f_B(1, n+1) + C_{31} f_A(1, n) &= 0, \\ B_2 f_B(2, n+2) + [H_{B,2}(n+1) - E] f_B(2, n+1) + C_{43} f_A(2, n) \\ + C_{42} f_B(1, n+1) + C_{41} f_A(1, n) &= 0, \end{aligned} \quad (4)$$

where the C_{ij} coefficients are the unknown matching coefficients. Using the procedure introduced by Kroemer and Zhu²¹ we now extend the wave functions defined in material A or B across the material boundary. For example, $f_A(1, n)$ which is defined at site n and $n-1$, can be defined (extended) at site $n+1$ using

$$A_1 f_A(1, n-1) + [H_{A,1}(n) - E] f_A(1, n) + A_1 f_A(1, n+1) = 0.$$

Substituting the extended wave functions in the system of Eq. (4) we obtain

$$\begin{aligned} -A_1 f_A(1, n+1) + C_{12} f_B(1, n+1) + C_{13} f_A(2, n) \\ + C_{14} f_B(2, n+1) &= 0, \end{aligned}$$

$$\begin{aligned} -B_1 f_B(1, n) + C_{21} f_A(1, n) + C_{23} f_A(2, n) + C_{24} f_B(2, n+1) \\ = 0, \end{aligned}$$

$$\begin{aligned} -A_2 f_A(2, n+1) + C_{34} f_B(2, n+1) + C_{32} f_B(1, n+1) \\ + C_{31} f_A(1, n) &= 0, \end{aligned}$$

$$\begin{aligned} -B_2 f_B(2, n) + C_{43} f_A(2, n) + C_{42} f_B(1, n+1) + C_{41} f_A(1, n) \\ = 0. \end{aligned}$$

Let us evaluate $f_A(1, m)$ and $f_A(2, m)$ for $n+1$,

$$\begin{aligned} f_A(1, n+1) &= \frac{C_{12}}{A_1} f_B(1, n+1) + \frac{C_{13}}{A_1} f_A(2, n) \\ &+ \frac{C_{14}}{A_1} f_B(2, n+1), \end{aligned} \quad (5)$$

$$\begin{aligned} f_A(2, n+1) &= \frac{C_{34}}{A_2} f_B(2, n+1) + \frac{C_{32}}{A_2} f_B(1, n+1) \\ &+ \frac{C_{31}}{A_2} f_A(1, n). \end{aligned} \quad (6)$$

Similarly let us evaluate $f_A(1, m)$ and $f_A(2, m)$ for $m=n$,

$$\begin{aligned} f_A(1, n) &= \frac{1}{\Delta} [C_{43} B_1 f_B(1, n) - C_{43} C_{24} f_B(2, n+1) \\ &- C_{23} B_2 f_B(2, n) + C_{23} C_{42} f_B(1, n+1)], \end{aligned} \quad (7)$$

$$f_A(2,n) = \frac{1}{\Delta} [C_{21}B_2f_B(2,n) - C_{21}C_{42}f_B(1,n+1) - C_{41}B_1f_B(1,n) + C_{41}C_{24}f_B(2,n+1)], \quad (8)$$

with $\Delta = C_{21}C_{43} - C_{41}C_{23}$.

The effective-mass matching theory applied to a single band with one Fourier coefficient states that the wave functions of material A and B at an interface located between $[n, n+1]$ verifies²¹

$$f_A(m) = \lambda f_B(m) \quad \text{for } m = n, n+1.$$

Under such conditions the band is the most transparent so that the transmission coefficient is maximized. To generalize this wave-matching technique to a two-band system, we now require the same linear dependence

$$f_A(1,m) = \lambda_{12}f_B(1,m) + \lambda_{14}f_B(2,m),$$

$$f_A(2,m) = \lambda_{32}f_B(1,m) + \lambda_{34}f_B(2,m),$$

to hold for both m equal n and $n+1$ across the interface of material A and B .

Enforcing this linear relationship at $n+1$ in Eqs. (5) and (6), we must have $C_{13} = C_{31} = 0$. Similarly enforcing this linear relationship at $n+1$ in Eqs. (7) and (8), we must have $C_{24} = C_{42} = 0$. It results that we can write at site n and $n+1$,

$$f_A(1,n) = \frac{1}{\Delta} [C_{43}B_1f_B(1,n) - C_{23}B_2f_B(2,n)],$$

$$f_A(2,n) = \frac{1}{\Delta} [-C_{41}B_1f_B(1,n) - C_{21}B_2f_B(2,n)].$$

$$f_A(1,n+1) = \frac{C_{12}}{A_1}f_B(1,n+1) + \frac{C_{14}}{A_1}f_B(2,n+1),$$

$$f_A(2,n+1) = \frac{C_{32}}{A_2}f_B(1,n+1) + \frac{C_{34}}{A_2}f_B(2,n+1).$$

Now enforcing the invariance of the λ_{ij} coefficient across the interface results in the following system:

$$\lambda_{12} = \frac{C_{12}}{A_1} = \frac{C_{43}B_1}{\Delta}, \quad (9)$$

$$\lambda_{14} = \frac{C_{14}}{A_1} = -\frac{C_{23}B_2}{\Delta}, \quad (10)$$

$$\lambda_{32} = \frac{C_{32}}{A_2} = -\frac{C_{41}B_1}{\Delta}, \quad (11)$$

$$\lambda_{34} = \frac{C_{34}}{A_2} = \frac{C_{21}B_2}{\Delta}. \quad (12)$$

First let us evaluate $|\Delta|^2$ from Eqs. (10) and (11),

$$\Delta = -\frac{C_{23}}{C_{14}}B_2A_1 = -\frac{C_{41}}{C_{32}}B_1A_2.$$

Using the Hermiticity property $C_{ij} = C_{ji}^*$ and the fact that the coefficients A_i are real, it results that

$$|\Delta|^2 = \Delta\Delta^* = A_1B_1A_2B_2. \quad (13)$$

Note that $A_1B_1A_2B_2$ must be a positive number. Inspection of AlAs, AsSb, InAs, InP, and GaAs bands¹⁶ reveals that their conduction bands have a minimum at Γ and an extremum at X so that the required condition is verified for these materials and their alloys.

One can easily verify that Eq. (12) can be derived from Eq. (9) using the result obtained for $|\Delta|^2$. Therefore, only three equations are independent in the system of four equations constituted by (9)–(12) and there will remain one arbitrary parameter that will characterize the junction.

To pursue the solution of Eqs. (9)–(11), let us now calculate the amplitude of Δ in terms of the C_{ij} coefficients,

$$\Delta = C_{21}C_{43} - C_{41}C_{23} = C_{21}\frac{\Delta C_{12}}{A_1B_1} + C_{41}\frac{\Delta C_{14}}{A_1B_2}. \quad (14)$$

It results using the Hermiticity property that we have

$$1 = \frac{|C_{12}|^2}{A_1B_1} + \frac{|C_{14}|^2}{A_1B_2}. \quad (15)$$

This establishes a relation between $|C_{14}|$ and $|C_{12}|$, namely,

$$|C_{14}|^2 = A_1B_2 \left[1 - \frac{|C_{12}|^2}{A_1B_1} \right]. \quad (16)$$

We wish to obtain a real solution for the C_{ij} since the coefficients A_i are real and a phase shift is without consequence on the current. Let us now consider two cases.

Case 1. A_1 , B_1 , A_2 , and B_2 are negative. Since all the A_i are negative, the products A_iA_j are also positive. Now since $|C_{14}|^2$ must be positive it results from Eq. (16) that we have

$$0 \leq |C_{12}|^2 \leq A_1B_1,$$

such that in turn we have

$$0 \leq |C_{14}|^2 \leq A_1B_2.$$

When the coefficient A_i are all negative it is natural (but not necessary) to select

$$C_{14} = -|C_{14}|,$$

and

$$C_{12} = -|C_{12}|.$$

Case 2. A_1 and B_1 are negative; A_2 and B_2 are positive. Since the product $A_1 B_2$ is negative and the product $A_1 B_1$ is positive, the property that $|C_{14}|$ must be positive requires that we have

$$|C_{12}|^2 \geq A_1 B_1 \geq 0.$$

Once C_{12} has been selected, C_{14} is known and the remaining coefficients can then be calculated as follow. First note that we are pursuing a solution where the coefficients C_{ij} are real numbers such that it results from Eq. (13) that we must have $\Delta = \pm \sqrt{A_1 B_1 A_2 B_2}$. Substituting Δ in Eqs. (9) and (10) gives then the final expression for the C_{43} and C_{23} coefficients, which depends on the sign of Δ ,

$$C_{43} = \pm C_{12} \sqrt{A_2 B_2 / A_1 B_1}, \quad C_{23} = \mp C_{14} \sqrt{B_1 A_2 / A_1 B_2}. \quad (17)$$

It was verified that the sign of Δ does not affect the amplitude of the transmission coefficient. It is natural, however, to select C_{43} to have the same sign as A_2 and B_2 .

Note that in absence of band coupling ($C_{13} = C_{23} = 0$), the coupling theory for C_{12} and C_{43} reduces to the effective-mass matching theory developed by Kroemer and Zhu²¹ for uncoupled tridiagonal Wannier bands.

We now present some numerical results demonstrating the application of this wave-matching theory to the coupling between the Γ and X valleys. The test structure is a RTD with 7 ML of GaAs spacers, 4 ML of AlAs barriers, and a 14-ML GaAs well. In this calculation, the Γ to X discontinuities are taken to be 0.48 and -0.92 eV for GaAs and AlAs, respectively. We have plotted in Fig. 1 the transmission coefficients obtained using an X -valley dispersion given by $A(1 - \cos ka)$ (Γ like) and in Fig. 2, the transmission coefficients obtained using an X -valley dispersion given by $A(1 + \cos ka)$ (X like). A coupling coefficient $C_{12}/\sqrt{A_1 B_1} = 0.99$ is used in Fig. 1. A coupling coefficient $C_{12}/\sqrt{A_1 B_1} = (0.99)^{-1}$ is used in Fig. 2.

The solid line corresponds to zero coupling, or equivalently a one-band model. Regular resonant-tunneling transmission peaks are observed to occur around 0.2 and 0.75 eV. The dashed and dotted lines correspond to the transmission probabilities in the Γ valley and X valley, respectively. Notice that there are two main features in Figs. 1 and 2 that deviate from the uncoupled result (solid line). The resonance/antiresonance around 0.3 eV is due to coupling through the X valley of AlAs. The resonance/antiresonance just below 0.5 eV is due to coupling to the X valley of GaAs. We will verify this assertion in the next section.

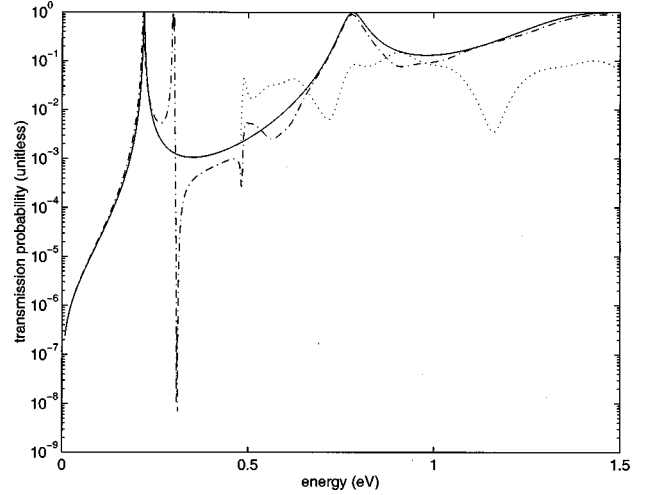


FIG. 1. Transmission coefficients versus incident energy obtained using an X -valley dispersions given by $A(1 - \cos ka)$ (Γ -like). The solid line corresponds to zero coupling (one-band model). The dashed and dotted lines correspond to the transmission probabilities in the Γ valley and X valley, respectively.

In Fig. 3, we have plotted the total (Γ plus X) transmission coefficient versus incident energy for various coupling coefficients $C_{12}/\sqrt{A_1 B_1}$ taking the values of 1 (no coupling), 0.999, 0.995, 0.99, 0.98. For a coupling coefficient of 0.999, the transmission coefficient (dashed-dotted line) approaches the one-band transmission coefficient (solid line). Clearly, the coupling and the magnitude of the coupling coefficient plays an important role. In Sec. V, we will use a full-band model to establish the coupling strength for a specific heterojunction.

In Fig. 4, we have plotted the total (Γ plus X) transmission coefficient versus incident kinetic energy of band 1 (Γ) in the emitter ($n = N_L$) $E_K = E - H$ ($b = 1$, $b' = 1$, $n' = N_L$, $n = N_L$, \mathbf{k}_\perp) for various values of the transverse wave vectors \mathbf{k}_\perp . In the Γ valley, the transverse wave vectors considered

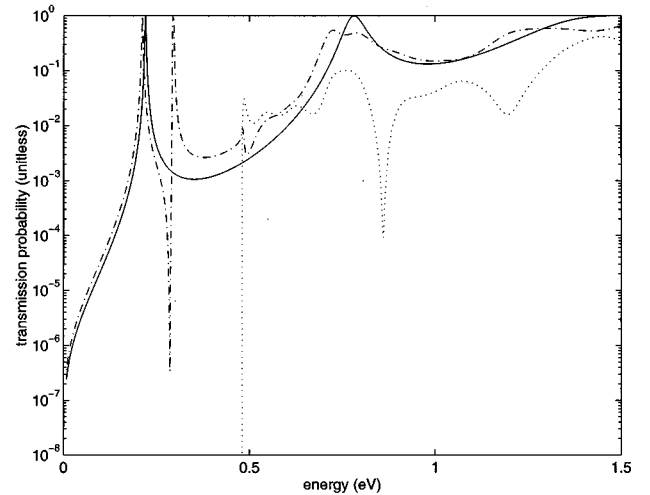


FIG. 2. Transmission coefficients versus incident energy obtained using an X -valley dispersions given by $A(1 + \cos ka)$ (X -like). The solid line corresponds to zero coupling (one-band model). The dashed and dotted lines correspond to the transmission probabilities in the Γ valley and X valley, respectively.

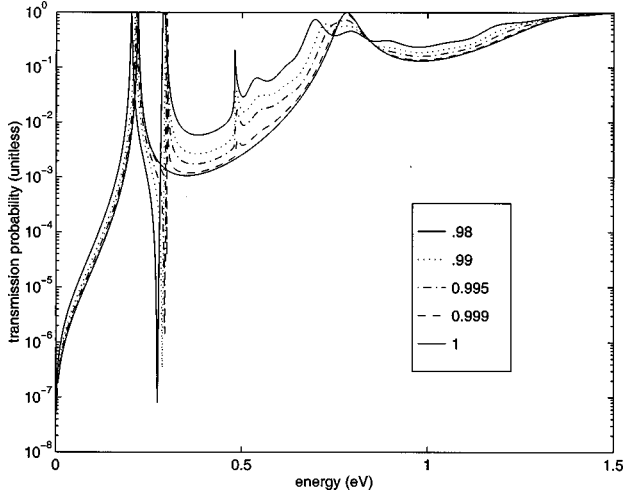


FIG. 3. Total (Γ plus X) transmission coefficient versus incident energy for various coupling coefficient taking the values of 1 (no coupling), 0.999, 0.995, 0.99, 0.98.

take the energies of 0, 0.05, 0.1, and 0.15 eV. A coupling coefficient of 0.99 is used in all the calculations. To demonstrate that the Γ resonance takes place for approximately the same kinetic energy $E_K = 0.21$ eV, we have multiplied the transmission coefficients by the factors (1, 10, 100, 1000) to separate them.

The resonances associated with the X valley in both AlAs and GaAs are seen to shift toward lower kinetic energies. The shift originates from the effective reduction with increasing transverse wave vectors of the Γ - X conduction band-edge discontinuity due to the much lower mass in the X valley compared to the Γ valley in both AlAs and GaAs. Clearly, the resonances/antiresonance will not occur at the same kinetic energies for various transverse wave vectors. This result will be useful when we discuss the impact of interface roughness scattering on the Γ - X resonances in Sec. VI.

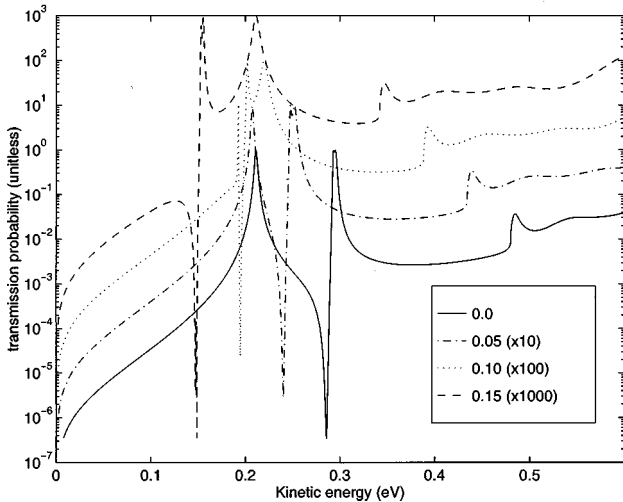


FIG. 4. Total (Γ plus X) transmission coefficient versus the incident kinetic energy E_K of the Γ band for various values of the transverse wave vectors. In the Γ valley the transverse wave vectors considered assume the energies of 0, 0.05, 0.1, and 0.15 eV. A coupling coefficient of 0.99 is used in all the calculations.

IV. MULTIBAND DENSITY OF STATES

To further analyze the simulation results obtained with the coupling theory derived above, it is useful to introduce a local density of states $N(E, n)$ at the lattice site n , which will permit us to locate in both position and energy the resonances and antiresonances present in that quantum structure. In equilibrium, the local total charge $\rho(n)$ is related to the local density of states (DOS) $N(E, n)$ according to

$$\rho(n) = \int f(E) N(E, n) dE, \quad (18)$$

with $f(E)$ the Fermi-Dirac function. We shall therefore derive the local multiband density function $N(E, n)$ by calculating the local total charge $\rho(n)$ in equilibrium. In general, the charge distribution in a ballistic quantum system is obtained by summing over all the individual charge distribution associated with the electrons injected in all the bands b' at the left L and right R contacts,

$$\rho(x) = \sum_{b'} [\rho_L(x, b') + \rho_R(x, b')],$$

where $\rho_{L/R}$ are given by

$$\rho_{L/R}(x, b') = \frac{2}{(2\pi)^3} \oint \oint \int_{k_{x,L/R}} f_{L/R}(E) |\psi_{L/R}(\mathbf{k}, x, b')|^2 d\mathbf{k},$$

with $f_{L/R}$ the Fermi-Dirac distribution in the left and right contacts.

In a multiband system the wave function $\psi_{L/R}(\mathbf{k}, x, b')$ can be expanded in terms of Wannier functions $w(b, n, \mathbf{k}_\perp)$ of the band b ,

$$\psi_{L/R}(\mathbf{k}, x, b') = \sum_b \sum_n f(b, n, b', \mathbf{k}) w(b, n, \mathbf{k}_\perp, x),$$

where we have $\mathbf{k} = (k_x, \mathbf{k}_\perp)$ with k_x either the longitudinal wave-vector incident on the left ($k_{x,L}$) or right ($k_{x,R}$) flat-band contact for ψ_L and ψ_R , respectively. Note that the transverse wave vector \mathbf{k}_\perp is translation invariant through out the device, unlike the contact wave vectors $k_{x,L/R}$.

Integrating the wave function ψ over x in the site interval $[a(n - \frac{1}{2}), a(n + \frac{1}{2})]$ and using the orthogonality of the Wannier functions of different bands together with their approximate locality around a single site, we obtain the following site average probability of presence:

$$\begin{aligned} |\psi_{L/R}(\mathbf{k}, n, b')|^2 &= \frac{1}{a} \int_{a(n-1/2)}^{a(n+1/2)} |\psi(\mathbf{k}, x, b')|^2 dx \\ &\approx \sum_b |f(b, n, b', \mathbf{k})|^2. \end{aligned}$$

We can now rewrite the site average charge distribution as a summation over the bands b and b' of the various wave-function contributions

$$\rho(n) = \sum_{b'} \sum_b [\rho_L(n, b, b') + \rho_R(n, b, b')],$$

where $\rho_{L/R}(n, b, b')$ is given by

$$\rho_{L/R}(n, b, b') = \frac{2}{(2\pi)^3} \int \int \int_{k_{x,L}} f_{L/R}(E) |f(b, n, b', \mathbf{k})|^2 d\mathbf{k}. \quad (19)$$

It can be verified that the envelope $f(b, n, b', \mathbf{k})$ can be related to the impulse response $h(b, n, b', n'', \mathbf{k})$. For waves $f(\mathbf{k}_L)$ injected in the left contact (site N_L), and for waves $f(\mathbf{k}_R)$ injected in the right contact (site N_R) in band b' , we have, respectively,

$$f(b, n, b', \mathbf{k}_{L/R}) = j \frac{\hbar v_{L/R}(b', E, \mathbf{k}_\perp)}{a} h(b, n, b', N_{L/R}, E, \mathbf{k}_\perp) \\ \text{for } n \leq N_R \text{ or } n \geq N_L,$$

where $v_{L/R}$ is the velocity of the wave injected from the left (L) or right (R) contact into the device ($v_{L/R}$ are selected to be positive).

The impulse response $h(b, n, b'', n'', E, \mathbf{k}_\perp)$ with total energy E and transverse wave vector \mathbf{k}_\perp for an excitation at site n'' in band b'' is obtained from the following multiband tridiagonal equation:

$$\sum_{b'=1}^{N_B} [H_-(b, b', n) h(b', n-1, b'', n'', E, \mathbf{k}_\perp) \\ + H_0(b, b', n, \mathbf{k}_\perp) h(b', n, b'', n'', E, \mathbf{k}_\perp) \\ + H_+(b, b', n) h(b', n+1, b'', n'', E, \mathbf{k}_\perp)] \\ = E h(b, n, b'', n'', E, \mathbf{k}_\perp) + \delta_{nn''} \delta_{bb''}.$$

We can now use this identity to rewrite the charge distribution $\rho_{L/R}(n, b, b')$ of Eq. 19

$$\rho_{L/R}(n, b, b') = \frac{2}{(2\pi)^3} \int \int \int_{k_{x,L/R}} f_{L/R}(E) |f(b, n, b', \mathbf{k})|^2 d\mathbf{k} \\ = \frac{2}{(2\pi)^3} \int \int \int_{k_{x,L/R}} f_{L/R}(E) \frac{\hbar^2 v_{L/R}^2(b', E, \mathbf{k}_\perp)}{a^2} |h(b, n, b', N_{R/L}, \mathbf{k})|^2 d\mathbf{k} \\ = \frac{1}{a^2} \frac{2}{(2\pi)^3} \int \int d\mathbf{k}_\perp \int_{-\infty}^{\infty} dE f_{L/R}(E) \hbar v_{L/R}(b', E, \mathbf{k}_\perp) |h(b, n, b', N_{R/L}, E, \mathbf{k}_\perp)|^2.$$

Due to the Hermiticity of the Hamiltonian and the associated current conservation property, these impulse functions verify the identity

$$-\frac{a}{\hbar} 2 \operatorname{Im}[h(b, n, b, n, E, \mathbf{k}_\perp)] \\ = \sum_{b'} v_L(b', k_{x,L}) |h(b, n, b', N_L, E, \mathbf{k}_\perp)|^2 \\ + v_R(b', k_{x,R}) |h(b, n, b', N_R, E, \mathbf{k}_\perp)|^2,$$

with $k_{x,R/L}$ obtained from $E = E(b, k_{x,R/L}, \mathbf{k}_\perp, N_{L/R})$. The equilibrium charge distribution is obtained for $f_L(E) = f_R(E) = f(E)$,

$$\rho(n) = \sum_{b'} \left[\sum_b \rho_L(n, b, b') + \rho_R(n, b, b') \right] \\ = -\frac{2}{a} \sum_b \frac{2}{(2\pi)^3} \int \int d\mathbf{k}_\perp \int_{-\infty}^{\infty} dE f(E) \\ \times \operatorname{Im}[h(b, n, b, n, E, \mathbf{k}_\perp)]$$

$$= -\frac{1}{a\pi} \int_{-\infty}^{\infty} dE f(E) \sum_b D_b \int_0^{\infty} dE_\perp \\ \times \operatorname{Im}[h(b, n, b, n, E, E_\perp)],$$

where we used the cylindrical symmetry to introduce $E_\perp = \hbar^2 k_\perp^2 / (2m_b^*)$ verifying $D_b dE_\perp = [2/(2\pi)^2] d\mathbf{k}_\perp$ with $D_b = m_b^* / \hbar^2 \pi$ the two-dimensional electron gas density of states in the band b .

Using Eq. (18), which relates the local charge $\rho(n)$ to the local density of state, we identify the local density of states $N(E, n)$ as

$$N(E, n) = \int_0^{\infty} N(E, E_\perp, n) dE_\perp,$$

with $N(E, E_\perp, n)$ the partial density of states in the channel E_\perp given by

$$N(E, E_\perp, n) = -\frac{1}{a\pi} \sum_b D_b \operatorname{Im}[h(b, n, b, n, E, E_\perp)].$$

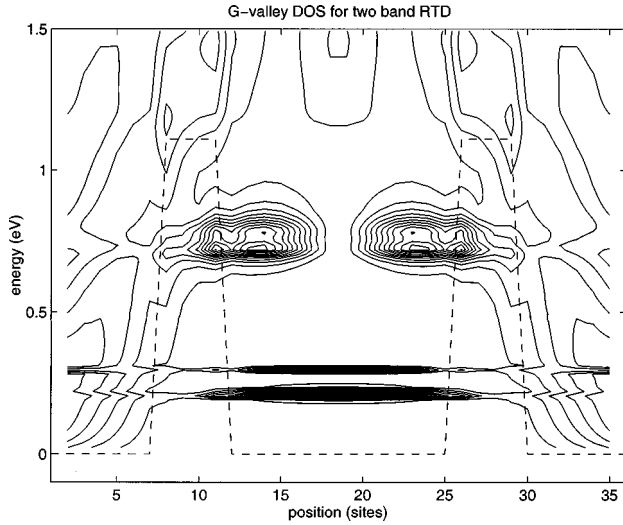


FIG. 5. Γ -valley density of states is plotted versus longitudinal energy and position for a zero transverse wave vector. The RTD structure and the X dispersion of Fig. 2 are used.

We will find more interesting to inspect $N(E, E_{\perp}, n)$ rather than $N(E)$ as we found in the heterostructure considered in Sec. III that the energy resonances and antiresonances can vary rapidly with the perpendicular energy E_{\perp} .

For the case of a heterostructure consisting of a single flat band,²² the impulse response $h(n, n', E, E_{\perp})$ is easily evaluated to be $h(n, n', E, E_{\perp}) = -ja/\hbar v(k_x)$, with k_x obtained from $E = E(b=1, k_x, k_{\perp}, n)$. Therefore, we have

$$N(E, E_{\perp}) = \frac{D_1}{\pi} \frac{1}{\hbar v(k_x)}.$$

We have verified that our simulator numerically reproduces this analytic result.

The multiband density of states formula derived above will help us now to establish the location and therefore the origin of the resonance and antiresonance in the RTD. For the purpose of this identification we will plot separately the impulse response $\text{Im}[h(b, n, b, n, E, E_{\perp})]$ of each band (valleys) b .

In Fig. 5, the Γ -valley density of states is plotted versus longitudinal energy and position for a zero transverse wave vector. In Fig. 6, the X -valley density of states is plotted versus longitudinal energy and position for a zero transverse wave vector. Notice that the density of states is zero below the X -valley minimum. Only the density of states contributing to the current are shown. The same test RTD structure as in Sec. III is used.

Science and art intersect in the Γ density of states, which has the appearance of a humanoid face. Notice the resonant ground state (no node) revealed as the bottom-high density structures (mouth) at about 0.2 eV and the first excited state (one node) as the two-top structure (eyes) at about 0.75 eV. One also notices a structure located midway (nose) at about 0.3 eV corresponding to the coupling between the Γ valley of the GaAs well and the X valley of the AlAs barrier as is clearly revealed by the X density of states shown in Fig. 6.

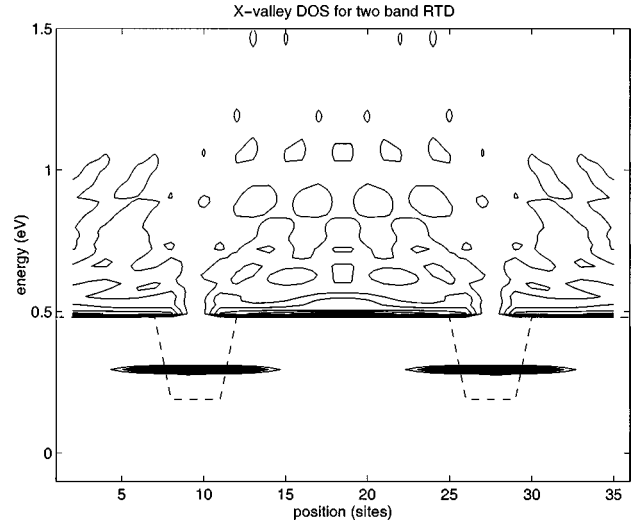


FIG. 6. X -valley density of states is plotted versus longitudinal energy and position for a zero transverse wave vector. The RTD structure and the X dispersion of Fig. 2 are used.

The X density of states features also an additional resonance just above the GaAs well and spacers.

The multiband Γ and X density of states permit therefore to identify both the band and spatial origin of the resonance and antiresonance resulting from the coupling of the Γ and X valleys.

V. COMPARISON WITH A FULL-BAND MODEL

Having introduced the two-band model and extended the effective-mass matching to such systems we shall now compare this simple two tridiagonal Wannier band system to a single full Wannier band model.

The single full Wannier band model used here is an improved version of the simulator reported in Ref. 7. This improved simulator, which can now handle heterostructures of useful size will be reported elsewhere.²⁰

Along the $\langle 100 \rangle$ direction the band structure is written

$$E(\mathbf{k}) = E(k_x, \mathbf{k}_{\perp}) = \sum_{p=1}^{N_W} H_p(\mathbf{k}_{\perp}) \cos\left(\frac{pk_x a}{2}\right), \quad (20)$$

with N_W the number of Fourier harmonics used.

The GaAs, AlAs, and $\text{Al}_{0.3}\text{Ga}_{0.7}\text{As}$ band structures along the $\langle 100 \rangle$ direction used in our comparison are shown in Fig. 7 for $\mathbf{k}_{\perp} = 0$. Ten Fourier coefficients $H_p(0)$ ($N_W = 10$) are used in our test to fit the bands. These Wannier bands GaAs and AlAs bands are obtained from a least-square fit of band-structure data obtained using a pseudopotential calculation.¹⁶ For the GaAs conduction band we added a small correction to bring the X valley 0.4 eV above the Γ valley (its initial value was 0.318 eV). The $\text{Al}_{0.3}\text{Ga}_{0.7}\text{As}$ band is obtained using a linear weighted average of the GaAs and AlAs bands. Care was placed in the least-square fit of the band data to obtain a very smooth X valley by fitting both the band structure and its second-order derivatives while maintaining exactly the mass and band discontinuities at the Γ and X points.

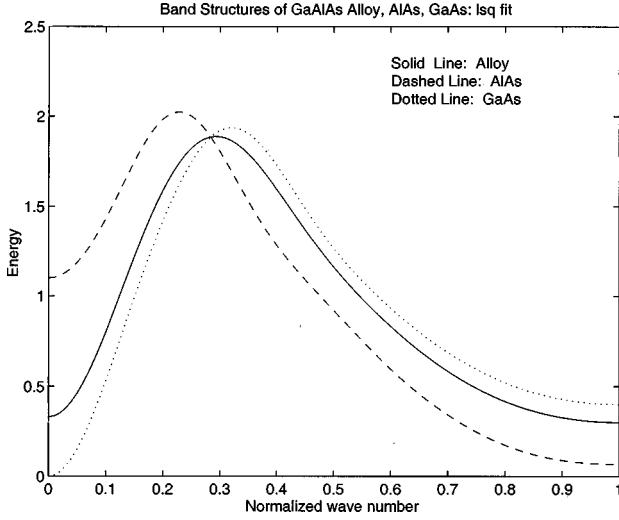


FIG. 7. Band-structures of $\text{Al}_{0.3}\text{Ga}_{0.7}\text{As}$ (solid line), GaAs (dotted), and AlAs (dashed-dotted line) plotted versus the normalized longitudinal wave vector $[k_x/(2\pi/a)]$ along the $\langle 100 \rangle$ direction for $\mathbf{k}_\perp = 0$.

To account in the coupled-band model for the noneffective mass in both the Γ and X valleys of the bands shown in Fig. 7 we use an energy- and position-dependent coefficient $A(b,n,E)$ in each of the tridiagonal band b of dispersion $E(k_x) = A(b,n,E)[1 \mp \cos(k_x a/2)]$. For energies for which the wave is propagating in the valley b [wave vector $k_x(b,n)$ with a zero imaginary part], $A(b,n,E)$ is selected to be

$$A(b,n,E) = \frac{E - E_{c,b}(n) - eV(n)}{1 \mp \cos[\text{Re}[k_x(b,n)]a/2]}. \quad (21)$$

For energies for which the wave is damped in the valley b [wave vector $k_x(b,n)$ with a nonzero imaginary part], $A(b,n,E)$ is selected to be

$$A(b,n,E) = \frac{E - E_{c,b}(n) - eV(n)}{1 - \cosh\{\text{Im}[k_x(b,n)]a/2\}}. \quad (22)$$

Note that the same expression is used for both the Γ - and X -damped waves. This originates from the fact that the real part of complex wave vector k_x is equal to π in the X valley and 0 in the Γ valley. In both Eqs. (21) and (22), $k_x(b,n)$ is the Γ and X wave vector associated with the solution of

$$E = E(k_x, \mathbf{k}_\perp) - eV(n), \quad (23)$$

where $E(k_x, \mathbf{k}_\perp)$ is the full-band structure, either GaAs or AlAs corresponding to the material at the lattice site n . Since we use 10 cosine harmonics in the full-band model to presents the GaAs, AlAs, and $\text{Al}_{0.3}\text{Ga}_{0.7}\text{As}$ band structures, the solution of Eq. (23) using analytical continuation leads to 20 complex numbers for the wave vector. Care was therefore placed in developing an algorithm automatically sorting these roots to identify the Γ and X roots for use in Eqs. (21) and (22) (the other roots are evanescent waves with very fast decays). This energy-dependent effective mass implements a

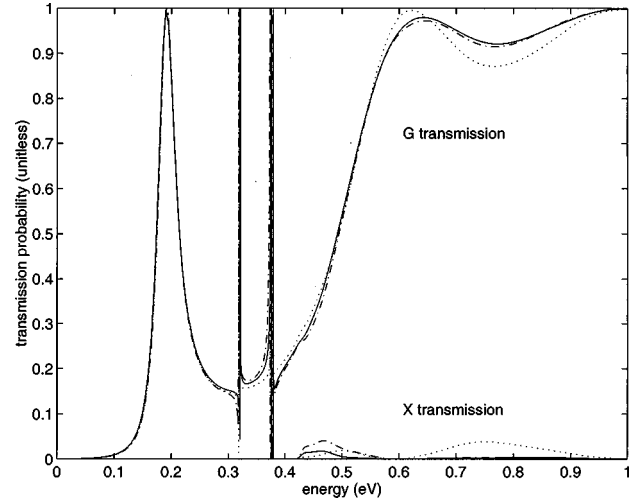


FIG. 8. Γ and X transmission coefficients versus incident energies obtained with the full-single band model (solid line), the effective-mass matching theory (dotted line), and the modified effective-mass matching theory (dashed-dotted line).

noneffective-mass correction, which as we shall see permits the resonances and antiresonances in the coupled-band model to occur at energies similar to those of the full-band model.

The interface matrix elements in the full-band model are selected using an arithmetic average.²⁰ Considering the limit of this approximation, we will only consider here GaAs- $\text{Al}_{0.3}\text{Ga}_{0.7}\text{As}$ RTD's, which are made up of very similar semiconductors (GaAs and $\text{Al}_{0.3}\text{Ga}_{0.7}\text{As}$) for which this interface Hamiltonian is a reasonable approximation.

In Fig. 8, we compare the Γ and X transmission coefficients versus incident energies obtained with the full-single band model (solid line), the effective-mass matching theory (dotted line). The test structure is a RTD with 7 ML of GaAs spacers, 8 ML of $\text{Al}_{0.3}\text{Ga}_{0.7}\text{As}$ barriers, and a 8-ML GaAs well.

Γ - X resonances are observed to take place for approximately the same energies. Some departures are observed, however, for the transmission to the X valley above 0.5 eV and the transmission to the Γ valley above 0.8 eV. An improved model is achieved by resetting the backward coupling coefficients to zero ($C_{23} = C_{32} = 0$) leaving all the other coefficients unchanged. The resulting Γ and X transmission coefficients (dashed-dotted lines) are now in better agreement at high energies.

A more detailed comparison of the resonances/antiresonances is shown in Fig. 9. Clearly the modified coupled-band model and the full-band model exhibits the same type of resonances indicating that the modified coupled-band model implements correctly the physical processes of the Γ - and X -valley coupling.

The improved fit points toward the limit of applicability of the effective-mass matching theory. However, as was pointed out by Kroemer and Zhu²¹ for the single-band model, departures from the ideal effect case of the effective-mass matching theory are to be expected and the effective-mass matching theory provides a reference to measure them.

Note that the same coupling ($\sqrt{A_1 B_1}/C_{12} = 0.999$) was used in both cases (dotted and dashed-dotted lines). This is a

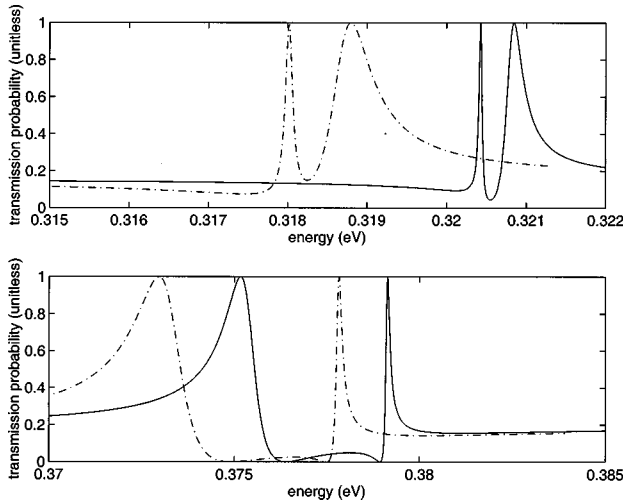


FIG. 9. Details of the Γ and X transmission coefficients for incident energies around the Γ - X resonance/antiresonance obtained using the full-single band model (solid line), and the modified effective-mass matching theory (dashed-dotted line).

relatively weak coupling since the single-band interface theory is recovered for $\sqrt{A_1 B_1}/C_{12}=1$. Note also that the X -valley dispersions $A(1 + \cos ka)$ (X -like) was used since the band structures used here (see Fig. 7) feature a minimum at X . The same coupling parameters were verified to provide an excellent fit as well for other GaAs-Al_{0.3}Ga_{0.7}As structures of different barrier and well widths.

VI. IMPACT OF INTERFACE ROUGHNESS

In real RTD's, the interfaces are not perfectly sharp but feature instead terraces typically of 1 ML thick and of various widths. This introduces a random fluctuation of the thickness of the barrier and well of the RTD. We demonstrate here the impact of interface roughness by calculating the ensemble average transmission coefficient following the procedure described in Refs. 23 and 24. In that procedure, interface roughness is treated as a virtual phase-breaking scattering process and each scattering event is assumed to be uncorrelated. For this purpose the self energy associated with the scattering process is added to both the Γ and X Hamiltonians. Current is verified to be conserved. Each scattered wave is calculated using the multiband impulse response developed in Sec. IV. The scattered waves are therefore also submitted to the interface coupling theory developed in this paper.

In Fig. 10 we compare the total (Γ plus X) transmission coefficients versus incident energies obtained with the one-band model (dotted line) the two-band model without interface roughness (dashed line), and the two-band model with interface roughness (plain line). The test RTD structure is the same as in Sec. III.

Interface roughness is seen to strongly impact the transmission coefficient. First the two normal resonant tunneling peaks at 0.3 and 0.75 eV exhibited by the one-band model (dotted line) are seen to have been shifted to lower energies due to the self energy associated with the Γ - X coupling (dashed line) and even more so by interface roughness scattering (plain line). In addition, the Γ - X resonance/

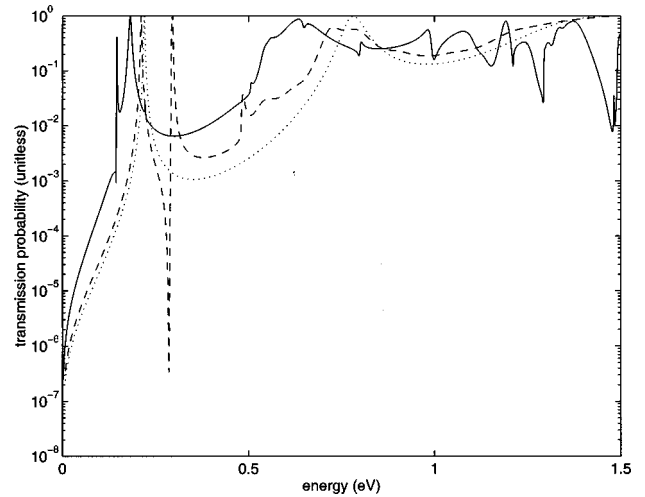


FIG. 10. Total (Γ plus X) transmission coefficients versus incident energies obtained with the one-band model (dotted line) the two-band model without interface roughness (dashed line), and the two-band model with interface roughness (plain line).

antiresonance observed at 0.3 and 0.5 eV in the two-band model (dashed line) seems to have been suppressed by interface roughness scattering (plain line). In fact they have contributed to the increase of the transmission coefficients in that range of energies. Note that the interface roughness scattering process while being an elastic process does deflect the trajectory of the incident electrons and can therefore convert the longitudinal energy of the electron into transverse wave-vector energy.²⁴ We have seen in Sec. III that the location of the Γ - X resonance/antiresonance varied rapidly with the transverse wave vector. The original Γ - X resonances/antiresonances of the two-band model (dashed line) could be considered to have been effectively suppressed by the ensemble averaging effect of the interface roughness scattering process.

An interesting effect is the appearance of a Γ - X resonance/antiresonance structure around 0.15 eV. This fine structure was verified to survive to two sequential scattering processes. The Γ - X resonance/antiresonance clearly arises from the resonant coupling of the Γ incident wave with the X -scattered waves generated via the interface roughness scattering process. The scattering process plays then the role of the coupling coefficient. Again the occurrence of the Γ - X resonance at lower energies is made possible by the effective lowering of the Γ - X conduction-band-edge discontinuities for the large transverse wave vectors of the scattered waves involved in interface roughness scattering.

VII. CONCLUSION

We have presented in this paper the extension of the effective-mass wave-matching theory developed by Kroemer and Zhu²¹ to a two-tridiagonal-bands Wannier system. The four independent coupling parameters of the two coupled tridiagonal bands system were found to reduce to a single parameter. The impact of this coupling parameter upon the transmission of electron in resonant tunneling diodes was studied for the case where this two-band system is applied to the modeling of the Γ and X valleys of a conduction band.

A general multiband density of states was derived to facilitate the location in space and energy of both the resonant tunneling resonances and the antiresonances. A general definition of current in a multiband system was also established to calculate the transmitted coefficients.

The application of this interface theory to a realistic situation was investigated by comparing simulation results obtained with the two tridiagonal-band interface theory and a single full-band model, which accounts for long-range interactions. A reasonable agreement was demonstrated for GaAs-Al_{0.3}Ga_{0.7}As resonant tunneling diodes (RTD's) using a noneffective-mass correction and a coupling factor of 0.999. An improved fit was further obtained by relaxing the backward interband coupling to zero. The modified coupling theory still only depends on a single-coupling parameter.

The resulting interface wave-matching model developed provides a simple yet realistic approach to account for both noneffective-mass effects and the coupling between the Γ and X or L valleys in the calculation of the transmission and reflection coefficients of RTD devices. The simplicity of the model makes also possible the study of the impact of multiple sequential scattering processes such as interface roughness scattering upon such multiband systems. The two-band Wannier model and the interface theory could also be potentially applied to other material or band systems.

ACKNOWLEDGMENTS

The authors would like to thank Dejan Jovanovich, Chris Bowen, and Roger Lake for fruitful discussions.

APPENDIX: MULTIBAND CURRENT DEFINITION AND CONSERVATION

In this appendix we establish a multiband definition of current and demonstrate its conservation. This is done below for a general tridiagonal system. Consider the equation satisfied by the envelope function of the band b ,

$$\sum_{b'} [H(b, b', n, n-1)f(b', n-1) + H(b, b', n, n)f(b', n) + H(b, b', n, n+1)f(b', n+1)] = Ef(b, n).$$

Multiplying this equation by $f^*(b, n)$, we obtain the new quantity R

$$R = \sum_{b'} [H(b, b', n, n-1)f^*(b, n)f(b', n-1) + H(b, b', n, n)f^*(b, n)f(b', n) + H(b, b', n, n+1)f^*(b, n)f(b', n+1)] = E|f(b, n)|^2.$$

Using the Hermiticity $H(b, b', n, n') = H(b', b, n', n)^*$ we derive

$$(R - R^*) = \sum_{b'} \{ \text{Im}[H(b, b', n, n-1)f^*(b, n)f(b', n-1)] + \text{Im}[H(b, b', n, n)f^*(b, n)f(b', n)] + \text{Im}[H(b, b', n, n+1)f^*(b, n)f(b', n+1)] \} = 0.$$

Let us now introduce the elemental current

$$j(b, b', n, n') = -\frac{a}{\hbar} \text{Im}[H(b, b', n, n')f^*(b, n)f(b', n')].$$

These elemental currents verify the conservation property,

$$0 = \sum_{b'} [j(b, b', n, n-1) + j(b, b', n, n) + j(b, b', n, n+1)]. \quad (\text{A1})$$

The current definition is now identified to be

$$J_T(n) = J_-(n-1, n) + J_+(n, n+1),$$

$$J_+(n, n+1) = \sum_b \sum_{b'} j(b, b', n, n+1),$$

$$J_-(n-1, n) = \sum_b \sum_{b'} j(b', b, n-1, n).$$

Let us now prove the current conservation. First, we note that we have

$$J_-(n-1, n) = J_+(n, n+1).$$

We therefore need to demonstrate that $J_-(n-1, n)$ or $J_+(n, n+1)$ is conserved from site to site. For this purpose we sum over the bands Eq. (A1),

$$\sum_b \sum_{b'} j(b, b', n, n-1) + j(b, b', n, n) + j(b, b', n, n+1) = 0. \quad (\text{A2})$$

This reduces to

$$\sum_b \sum_{b'} j(b', b, n-1, n) = \sum_b \sum_{b'} j(b, b', n, n+1).$$

Now using the Hermiticity of the Hamiltonian, the elemental currents one easily verifies the identity $j(b', b, n', n) = -j(b, b', n, n')$. It results in the following identity

$$\sum_b \sum_{b'} j(b, b', n, n) = 0.$$

Equation (A2) reduces then to

$$\sum_b \sum_{b'} j(b', b, n-1, n) = \sum_b \sum_{b'} j(b, b', n, n+1),$$

which demonstrates the current conservation throughout the heterostructures. Note finally that this definition of current reduces to the conventional definition of current in a Wannier band in the contacts where the bands are decoupled.

*FAX: (614) 292-7596. Electronic address:

roblin@ee.eng.ohio-state.edu; URL: <http://eewww.eng.ohio-state.edu/~roblin>

¹R. Lake and S. Datta, Phys. Rev. B **45**, 6670 (1992).

²P. Sotirelis and P. Roblin, Phys. Rev. B **51**, 13 381 (1995).

³E. R. Brown, J. R. Söderström, C. D. Parker, L. J. Mahoney, K. M. Molvar, and T. C. McGill, Appl. Phys. Lett. **58**, 2291 (1991).

⁴H. C. Liu and T. C. L. G. Sollner, Semicond. Semimet. **41**, 359 (1994).

⁵A. Rydberg and H. Grönqvist, Electron. Lett. **25**, 348 (1989).

- ⁶D. Y. K. Ko and J. C. Inkson, Phys. Rev. B **38**, 9945 (1988); Semicond. Sci. Technol. **3**, 791 (1988).
- ⁷P. Roblin, Superlattices Microstruct. **4**, 363 (1988).
- ⁸Kenneth V. Rousseau, K. L. Wang, and J. N. Schulman, Appl. Phys. Lett. **54**, 1341 (1989).
- ⁹D. Z.-Y. Ting, E. T. Yu, and T. C. McGill, Phys. Rev. B **45**, 3583 (1992).
- ¹⁰T. B. Boykin and J. S. Harris, J. Appl. Phys. **72**, 988 (1992).
- ¹¹R. C. Bowen, W. R. Frensley, G. Klimeck, and R. K. Lake, Phys. Rev. B **52**, 2754 (1995).
- ¹²P. Vogl, H. P. Hjalmarson, and J. D. Dow, J. Chem. Solids **44**, 365 (1983).
- ¹³J. Schulman and Y. C. Chang, Phys. Rev. B **31**, 2056 (1985).
- ¹⁴W. Harrison, *Electronic Structure and the Properties of Solids, the Physics of Chemical Bond* (Freeman, San Francisco, 1980).
- ¹⁵T. B. Boykin, Phys. Rev. B **54**, 8107 (1996).
- ¹⁶M. L. Cohen and T. K. Bergstresser, Phys. Rev. **141**, 789 (1963).
- ¹⁷K. Mader and A. Zunger, Phys. Rev. B **50**, 17 393 (1994).
- ¹⁸J. G. Gay and J. R. Smith, Phys. Rev. B **11**, 4906 (1975).
- ¹⁹P. Roblin and W. R. Muller, Phys. Rev. B **32**, 5222 (1985).
- ²⁰J. G. Cao and P. Roblin (unpublished).
- ²¹H. Kroemer and Qi-Gao Zhu, J. Vac. Sci. Technol. **21**, 551 (1982).
- ²²P. R. thanks Dr. Lake of Texas Instrument for introducing him to the single-band DOS definition.
- ²³P. Roblin and W. R. Liou, Phys. Rev. B **47**, 2146 (1993).
- ²⁴P. Roblin, R. C. Potter, and A. Fathimulla, J. Appl. Phys. **79**, 2502 (1996).